Conclusions

The large hadron collider will be a powerful tool for discovering new Physics provided the generated events can accurately be observed, but its harsh environment will be a major concern for the operation of large scale detectors. Since monocrystalline silicon microstrip detectors provide the required position accuracy, and as the RD48 collaboration developed a powerful empirical model to describe the evolution of their most critical properties, these detectors are a first class choice for the tracking at LHC.

The large scale of the experiments, their large number of channels and the vast amount of microstrip detectors needed to build the tracker oblige the collaborations to monitor the quality during the sensor production. Therefore, after a long R&D program aimed to the design of the detectors, the CMS collaboration set up a complete QA scheme. This program included, among other tests, radiation hardness tests to ensure a constant quality of the detectors. The radiation tests were dedicated to and focused on the evolution of macroscopic properties, comparing this evolution to the model developed by the RD48 collaboration.

In that scope, this work presents the efforts done in Louvain to assemble and calibrate the necessary equipment required to perform the electrical characterization on one hand, and the tools required for the irradiation of silicon microstrip sensors under an intense fast neutron flux on the other hand. The neutron beam was developed during the preceding years. Additional equipment and dosimetry methods were also developed and are presented as annexes of the document.

All the instruments and methods developed during the last few years give a valuable experience to the lab in various domains. In the different measurements required to characterize a silicon detector of course, but also in the dosimetry of the neutron beam; in the control of irradiation parameters; in post-irradiation thermal treatment or the handling of detectors in general.

The experimental measurements present different results. A side experiment that had to be made to confidently use the NIEL scaling hypothesis during the irradiation tests was the measurement of k-factors for neutrons above 20 MeV. Indeed, most of the fast neutrons of the Louvain-la-Neuve beam have energies above 20 MeV, but there is no experimental measurement of k-factors above that energy. Standard silicon diodes have therefore been irradiated with the UCL monoenergetic neutron beam at three different peak energies. The results of these irradiations show differences with the usual curve, but the large relative errors on the obtained factors do not allow to conclude for a significant deviation from the predictions.

The low gamma and charged particle contamination of the Louvain neutron beam allows the biasing of the detectors during irradiation. This is generally not the case with beams used for radiation hardness tests purposes. This is obviously due to the fact that charged particle beams lead to a very high charge carrier density within the bulk of the device during irradiation. This would lead to destructive currents if the device is biased at that moment. Hence, we studied the influence of bias during irradiation on a sample of devices. Our study shows that there is no evidence of the bias influence on the evolution of the macroscopic properties of silicon sensors.

However, part of this study unveiled a long term effect: the depletion voltage of a sensor seems to rise when biased for a long time, even at LHC operating temperature. Previously mentioned only once in the literature, a confirmation of this effect, its reproducibility and impact on the operation of a tracker module would be an interesting perspective and could be a concern.

The initial goal being to get involved in the CMS QA scheme, the major part of the irradiations were dedicated to the testing of the sensor production to monitor the evolution of their electrical properties in a standard way. The results gathered on more than 300 structures give a statistical basis to the validation of the Hamburg model coefficients used to predict the evolution of the depletion voltage and the leakage current of the sensors along their use in CMS. The study also showed that the other electrical properties do not significantly degrade at high fluences, the interstrip capacitance of thick sensors being the only parameters found to significantly evolve.

The interstrip capacitances of thick sensors have indeed shown to present a late saturation value at a bias voltage that is high above the depletion voltage of the detector. The interstrip capacitance-bias voltage curve shows a first plateau around the depletion voltage at a capacitance value higher than expected. This effect may have only little influence on the crosstalk between channels, but there are no detailed study about it to our knowledge. In addition, this effect could be studied as another interesting effect of radiation on the sensors: considering other coatings than SiO_2 for the surface of the sensors may lead to different surface defects, inducing another behaviour of the interstrip capacitance.

Annexes

A.1. Dosimetry and fluence calculations

The estimation of the fluence obtained with the different beams and the dose delivered to the silicon sensors during irradiation is, as discussed above, a crucial step in the radiation hardness tests. This part of the annexes describes the dosimetry methods and the other means used to determine these fluences, as well as their calibration.

A.1.1. Beam monitor

With the direct measurement and the integration of the deuteron current on the neutron production target, and with the help of the beam properties studied in [48], we perform the online monitoring and calculation of the attained fluence (Fig. 89).

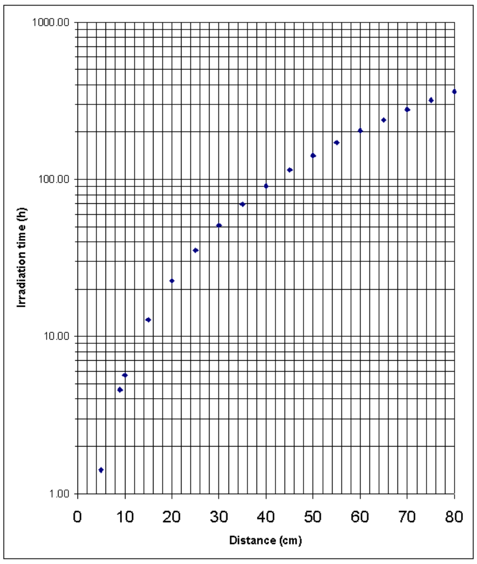

Fig. 89 : Time required to get 10^{14} n/cm^2 (not 1 MeV-equivalent) in the T2 neutron beam line with a deuteron current of 1 μA.

This monitoring is using lab-made floating current digitizers previously designed in the context of MSGC tests. These devices are built to measure currents as low as 10 nA, as high as 100 µA and are therefore well suited for this beam monitoring purpose. It is equipped with an analogue voltage output and a frequency output, both of these are well suited to our Keithley acquisition card and to a scaler installed in the same NIM crate as the current digitizer.

Before starting any silicon sensor irradiation test, we checked the current calibration of its outputs using a voltage source and a resistor. Knowing the value of the resistor with variable voltages, we know the current that should be read by the current digitizer.

The frequency calibration, counted by the attached scaler, gave a factor of 360870 counts/µAh. We are then able to obtain the calibration of our DAQ card readings, as shown in Fig. 90.

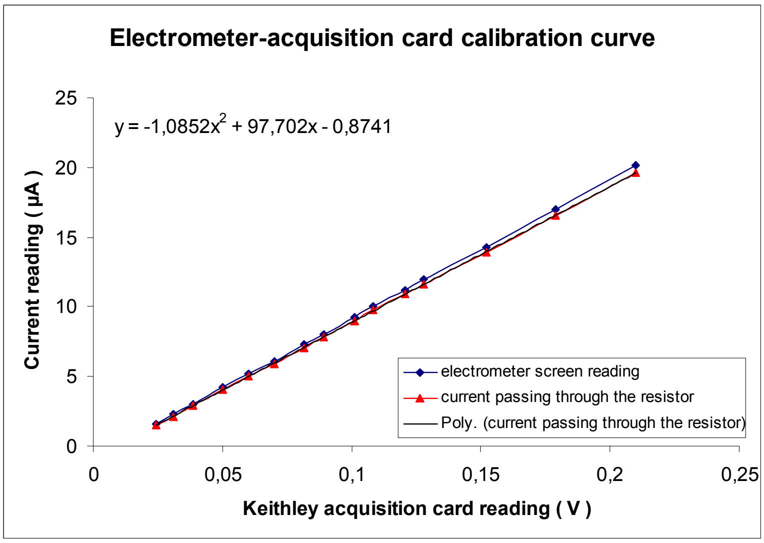

Fig. 90 : Keithley acquisition card and electrometer calibration curves.

This conversion has been incorporated in the irradiation-monitoring program in addition to the temperature readings and sensor power supply controls. It allows an online estimation of the fluence, complementary to the other post-irradiation dosimetry techniques described in the following paragraphs.

A.1.2. Activation

At the beginning of our sensor tests, we used activation foils to compute absolute neutrons fluxes at several different energies to check previous results on the neutron beam energy spectrum and confirmed the dosimetry results obtained either by the beam monitoring (see the above paragraph) or by the alanine system (cf. below).

Principle

The use of activation foils made of several different materials to determine the neutron spectrum in the T2 beam line has been discussed in a detailed way in [48] and another discussion can be found in the ASTM notice E720 [56]. We will therefore not go in such a detailed study here, but only remind its different steps.

The principle is to detect the gamma rays following the decay of radioisotopes produced during irradiation with neutrons.

At a given time T after the irradiation, the activity of a foil induced by the nuclear reaction "a" is given by:

$$A_a(T) = N_0 \overline{\sigma_a \phi}\left(1 - e^{-\lambda_a t_{irr}}\right)e^{-\lambda_a T} \qquad (\text{A.1})$$

Where N_0 is the number of atom of the relevant isotope in the foil (supposed to be uniformly irradiated), $\overline{\sigma_a \phi}$ is the reaction cross section integrated over the incident energy spectrum, λ_a the lifetime of the specific reaction product and t_{irr} the irradiation duration.

Knowing the incident neutron energy spectrum $d\Phi(E)/dE$, we compute an average cross section for a given reaction

$$\Phi_{tot} = \int_E \frac{d\Phi(E)}{dE} dE \qquad (\text{A.2})$$

$$\overline{\sigma_a} = \frac{\int_E \frac{d\Phi(E)}{dE}\sigma_a(E)dE}{\Phi_{tot}} \qquad (A.3)$$

Then, we make the following assumptions:

$$\overline{\sigma_a \phi} = \overline{\sigma_a}\phi_a \qquad (A.4)$$

ϕ_a being the neutron flux in he energy bin where σ_a is not negligible.

This allows us to use (A.1) and the activation foil activity to compute the total neutron flux in an energy range specific to the production of a given radionuclide (A.5).

$$\phi_a = \frac{A_a(T)}{N_0\overline{\sigma_a}\left(1-e^{-\lambda_a t_{irr}}\right)e^{-\lambda_a T}} \qquad (A.5)$$

In the case where the counting of the activity is made over a time lapse t_c and the number of counts is N_c, the experimental determination of the activity can be written as:

$$A_a^{\exp}(T) = \frac{N_c\lambda_a}{(1-e^{-\lambda_a t_c})} \qquad (A.6)$$

This leads to the following expression of the fluence:

$$\Phi_a = \frac{N_c\lambda_a}{N_0\overline{\sigma_a}\left(1-e^{-\lambda_a t_{irr}}\right)e^{-\lambda_a T}\left(1-e^{-\lambda_a t_c}\right)} \qquad (A.7)$$

In addition, the number of counts needed to get the experimental activity of the sample is corrected by the absolute detector efficiency (next paragraph) and dead time.

Calibration of the HPGE detector

A previous calibration of the HPGE detector has been carried out in [48] and repeated many times afterwards. It uses a well-known ^{152}Eu reference source. The results of the latest calibration, together with previous ones, are plotted above in Fig. 91.

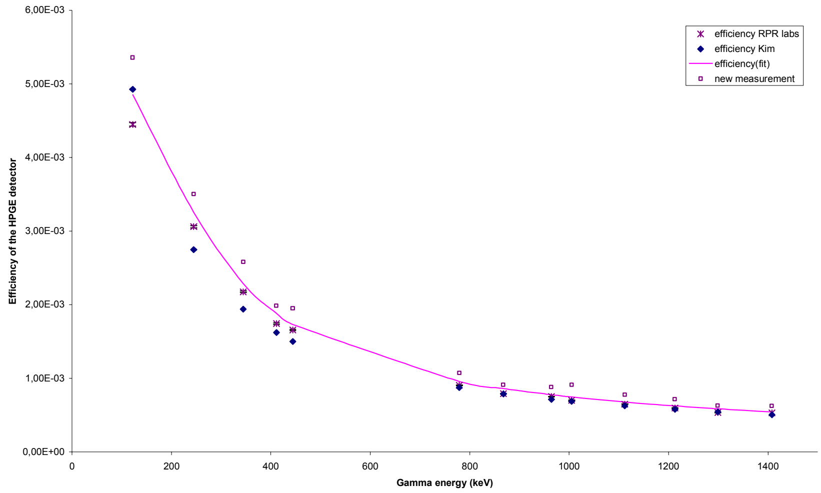

Fig. 91 : Efficiency of the Canberra HPGE detector.

Reactions considered

Using activation foils, one has always to consider several nuclear reactions with different thresholds to cover the full neutron energy spectrum. Table 23 gives an overview of the foils used here and the nuclear reactions involved.

Using Co foils, we could also use the $^{59}Co(n,\gamma)^{60}Co$ reaction, yielding gammas at 1173 and 1332 keV, but these do not allow multiple use of the activation foil due to the relatively long-lived ^{60}Co (5.27 y). On the other hand, the short-lived (1.5 d) $^{58}Ni(n,2n)^{57}Ni$ reaction is also unusable during our irradiation test.

Reaction	Incident neutron energy range (MeV)	Natural abundance of the initial isotope	γ energy (keV)	Gamma ray intensity	T ½ (days)
$^{58}Ni(n,p)^{58}Co$	2 – 20	0,683	811	0.995	70.916
$^{59}Co(n,2n)^{58}Co$	14 – 50	1	811	0.995	70.916
$^{59}Co(n,3n)^{57}Co$	> 20	1	122	0.855	271.77
$^{93}Nb(n,2n)^{92m}Nb$	9 – 30	1	934	0.991	10.15

Table 23 : Reactions of interest in the T2 beam line activation measurements.

Results

This method gave results consistent with the energy ranges of the 4 different reactions.

As an example, for a fluence estimated to 1.1 10^{14} n.cm^2 by the beam monitoring:

- the Nb(n,2n) reaction gave 10^{14} n/cm^2 (covering almost the whole energy spectrum) ;
- the Ni reaction gave 4.2 10^{13} n/cm^2 (covering almost the first half of the spectrum) whereas the Co(n,3n) reaction, its complementary, gave 7,32 10^{13} n/cm^2 for the high energy part.

A.1.3. Alanine

In addition to the evaluation of the fluence, we used individual dosimeters for each silicon sensor or test structure. The reason is twofold: first, we wanted to detect any beam misalignment of the sensors and second, because the beam distribution is not uniform across its spot.

An individual dosimetry system does help to disentangle huge fluence discrepancies due to any stack misalignment: it is not detectable with the beam monitoring alone. It also helps to take the beam radial dose distribution into account.

Considering the different dosimetry systems readily available, alanine seemed to be one of the most efficient one:

- Films are easy to handle but pellets can also be considered using the same reader.

- The dose range is wide (from 10 Gy up to 500 kGy with our films), making it suitable for other intense radiation fields.

- As alanine dosimetry is based on the generation of free radicals within the film by radiation*, there is little fading [57] in contrast to e.g. thermoluminescent dosimeters (an introduction can be found e.g. in [1]). We can therefore keep track of the doses by storing the dosimeters and can re-measure these ones in case it is needed.

- Although alanine is mainly used for Gamma ray induced dose measurements, it is also sensitive to neutrons (see e.g. [58]) and protons or other charged particles. In this case, one needs to know the Relative Effectiveness** (R.E.) of alanine for the considered radiation. It then allows cross checks between laboratories using different beams.

One important characteristic to be mentioned is that its response to the radiations varies with the ambient temperature during exposure. This can easily be taken into account in our case as the Bruker E-scan reader (Fig. 92) includes automatic correction of the readings.

The disadvantage of alanine is that, as previously mentioned, it is mainly used for gamma-ray dosimetry (and especially ^{60}Co, one of the most common high intensity gamma ray source). The dose read by our commercial system after neutron exposure may therefore differ from the tissue-equivalent neutron dose, and the fluence-to-dose factor may also vary between dosimetry systems.

* Alanine dosimetry is based on the quantification of these free radicals by detection of their free electrons using Electron Paramagnetic Resonance (EPR).

** The Relative Effectiveness (R.E.) is defined as the ratio of dosimeter signal after equal doses of considered radiation and reference radiation, usually ^{60}Co (for which our system is designed).

Fig. 92 : The Bruker E-scan alanine reader.

Study of a fluence-to-dose conversion factor

Using the beam monitoring, we computed the fluence-to-dose conversion factor for Kodak BioMax dosimeters irradiated in our high flux neutron beam. We checked how this conversion factor compares with the few references either found in data compilations on dosimetry systems or starting back with the corresponding KERMA coefficients.

To determine our experimental factor, we placed several dosimeters right in the center of the beam, at a distance larger than 50 cm from the production target to ensure a uniform irradiation. The beam fluence has been determined using the beam profile as described in section A.1.1. The obtained conversion factor is of 4.51 fGy.m^2, with a standard deviation of 9.8 %, in good agreement with the errors on the computation of the fluence.

Given this experimental factor, we compare it to the computations of response factors obtained using the T2 beam line energy spectrum (as described in [48]) folded with the alanine response function (Fig. 93, taken from Tavlet et Al in ref. [59]) using (A.8).

$$resp_{beam} = \frac{\int_E \frac{d\Phi(E)}{dE} resp(E) dE}{\int_E \frac{d\Phi(E)}{dE} dE} = \frac{\int_E \frac{d\Phi(E)}{dE} resp(E) dE}{\Phi_{tot}} \qquad \text{(A.8)}$$

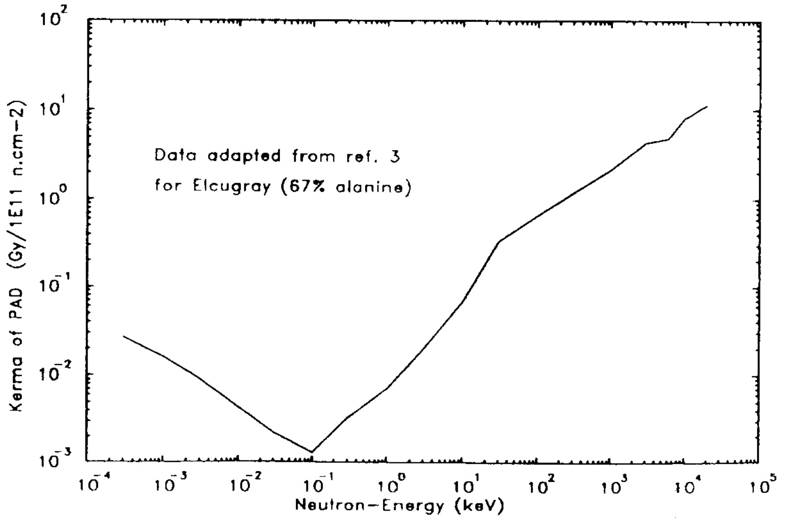

Fig. 93 : Response of PAD-Elcugray to neutrons as taken from [59].

This second method gave a fluence-to-dose conversion factor of 4.06 fGy.m^2.

In a similar way, one can fold the neutron spectrum to the KERMA coefficients determined by Chadwick et al. [60] and experimentally corrected by Meulders et al. [61]. In the latter case, we start by computing the neutron KERMA at the relevant energies using the alanine chemical formula ($C_3H_7NO_2$) and then fold it with the neutron energy spectrum and the relative effectiveness (R.E.) of alanine in a way similar to (A.8).

The R.E. of alanine can be found e.g. in Waligorski et al. [62], or Gertsenberg et al. [63]. The R.E. quoted in the latter (pictured in Fig. 94) are closer to the 0.36-0.7 range mentioned by Schraube et al [64].

The results are summarized in Table 24, where the third column shows factors computed using the Waligorski R.E. whereas the fifth uses the Gertsenberg spectrum.

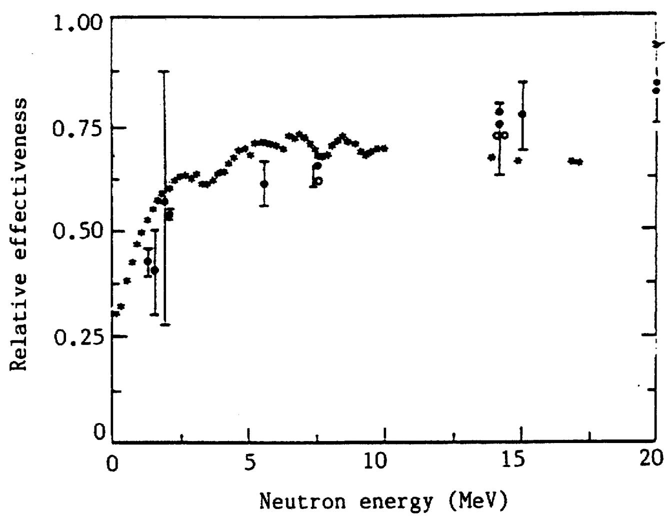

Fig. 94 : Alanine relative effectiveness to neutrons taken from [63].

	KERMA ($fGy.m^2$)	R.E. (Wal.)	Alanine response ($fGy.m^2$)	R.E. (Gert.)	Alanine response ($fGy.m^2$)
Chadwick	6.14	0.75	4.61	0.7	4.29
Meulders & Chadwick	6.16	0.75	4.62	0.7	4.31
Average	6.13	/	4.61	/	4.3

Table 24 : Alanine fluence-to-dose conversion factors obtained using literature (cf. [60], [61], [62] and [63]).

We conclude that our value of 4.51 ± 0.44 $fGy.m^2$ for the fluence-to-dose conversion factor for Kodak BioMax dosimeters shows a good agreement with computations based on existing literature. Although we have no indication of their exact chemical composition, the second method, starting with the KERMA, gives results that are closer to our experimental factor.

However, with respect to R.E. factors quoted in the literature, our measurements are not accurate enough to confirm either results obtained by Waligorski [62] or those quoted by Gertsenberg [63] or Schraube [64].

Despite the fact that the factor computed using the M. Tavlet data differs more from our experimental result, both methods are, in our case, complementary as we do not have the detailed chemical composition of our Kodak Biomax dosimeters*. In fact, the alanine response to neutrons depends on the binder used to make the dosimeters: on its alanine/paraffin ratio in case paraffin is used as a cement for alanine powder (the KERMA of neutrons into the material changes, as discussed in [64]), and one can therefore easily introduce uncertainties.

Remarks on the alanine response to protons

In collaboration with colleagues of the CMS silicon sensor group in Karlsruhe, we asked them to irradiate some of our alanine films with their 24 MeV proton beam.

The dose readings are, of course, much more important with respect to the fluences as we deal here with charged particles. Assuming the R.E. of alanine is 1 for protons above 15 MeV [62] and a radiation effectiveness weighting factor of 5 (cf. G. F. Knoll, [1]), the particle data group [65] gives a fluence-to-dose conversion factor about 46 fGy.m^2 for 50 MeV protons.

Only two dosimeters irradiated gave a consistent experimental factor obtained, of 67.4 fGy.m^2. This result is plotted together with PDG data in Fig. 95. Two other dosimeters gave factors even bigger than 100 fGy.m^2.

* We only know the strip on which the dosimeter is glued is made of PET ($C_{10}H_{10}O_4$)

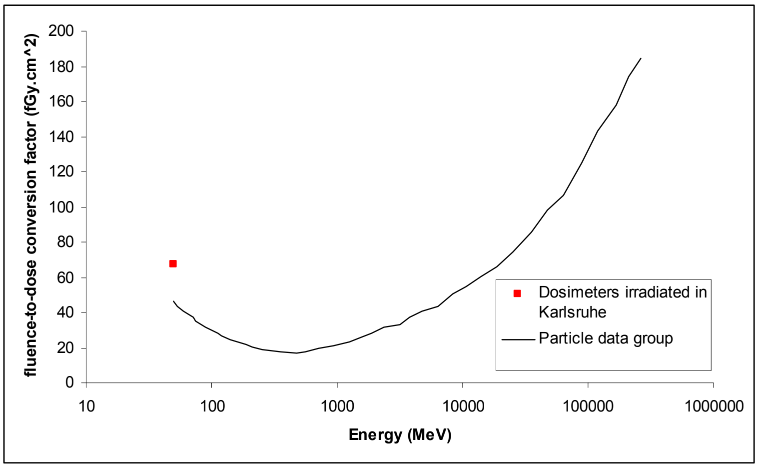

Fig. 95 : Alanine fluence-to-dose conversion factors for protons.

As our experimental factor is pretty different to the quoted ones, and since there are big differences with some other dosimeter readings, further investigations on this topic have to be envisaged.

A possible way to explain the difference is the dose rate encountered by these dosimeters during irradiation: as mentioned in the ASTM notice on alanine [66], the dose rate for alanine in a continuous radiation field has to be lower than 100 Gy/s, and our dosimeters get their full dose (more than 80 kGy) in less than 365 s. This leads to a minimum dose rate of 220 Gy/s, twice the recommended maximum one.

Within this scope, further information on the alanine response to protons can be found in references [67] through [70].

Remark on encountered problem with our Bruker E-scan

From time to time, we have an error message from the alanine readout system during the instrument check, right before any measurement: “Error 112 – frequency out of range: samples removed?”.

This message may appear when the sample holder is not in place, or its positioning is bad. Here however, it seems the problem arises is due to important temperature changes in the lab: the resonant frequency of the apparatus is affected and gets offset by a few kHz out of the allowed limit given by the previous calibration.

Although we monitored the temperature for several weeks during summer and winter and didn't observe the problem again as the temperature drops or increases, this error message can still happen, and we feel important to write here the way to fix it and keep the system running.

The solution to this problem is in fact to recalibrate the system. This requires the readings of NIST-traceable dosimeters if you want not to loose the system absolute calibration and can be annoying if your dosimeter set has been unused for several months because of the small fading they have anyway.

To avoid either to buy new calibrated dosimeters or to risk loosing the system calibration, one has to run the calibrate.vbs script again, but only perform an instrument check. Thereafter, select the "modify an existing calibration" option, load the existing one and perform the fitting again.

In this way, the routine merely establishes the reference values for the instrument self check but will not affect the performance of the instrument or change the alanine calibration curve.

A.2. Thermal treatment of the sensors: annealing oven

Many times, we stressed out the annealing-dependent time evolution of the properties of our silicon devices. This has particularly been emphasised for leakage currents or depletion voltages.

Therefore, any radiation-related study of silicon diode or sensor properties requires a good control of the device's annealing state. This can only be done using an oven with high temperature stability, which also doesn't vary too much during openings for structure introduction and/or removal.

As any commercial oven is an expensive piece of equipment, we designed a dedicated small oven (pictured in Fig. 96) whose characteristics are described below.

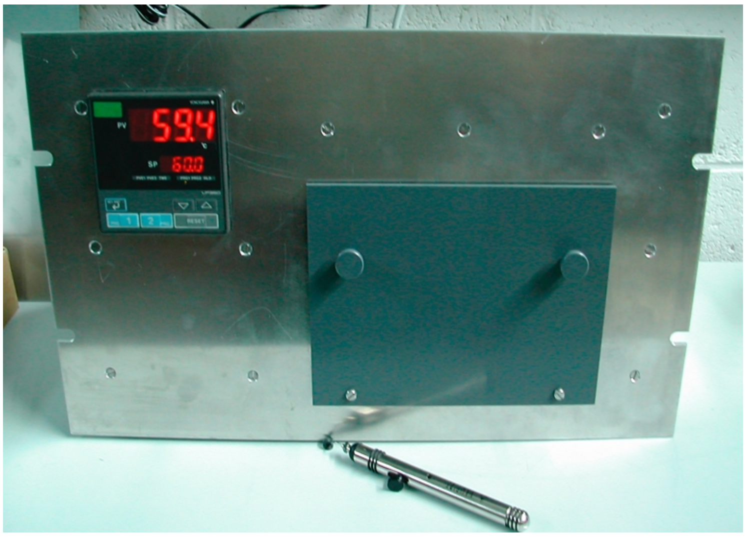

Fig. 96 : Annealing oven.

A.2.1. Principle

The most important characteristic of an oven for silicon annealing is the temperature stability. It does not require having a fast response time since the heat treatments are made at constant temperatures and because it is much easier to put the structures inside and remove these when the required annealing time is reached.

Ensuring a good temperature stability means that the oven specific heat must be high, the air volume is kept as small as possible and, of course, the thermal insulation is as good as achievable.

We choose to use special insulating bricks to ensure the first and the latter criteria. This solution had proven to be efficient with a previously built oven for TLD-annealing. A dedicated kitchen jolt resistor, directly connected to the mains using a power relay, ensures the heating of these heavy bricks.

The temperature regulation is made by a Yokogawa UP-350 programmable controller [71]. This is a very simple way to control the temperature since these modules are equipped for reading of Pt100. They provide a display showing the temperature setting and the measured current temperature. Electrical connections (cf. sketch on Fig. 97) are also easy to make and the auto-tune functionality quickly makes the oven operational in the best conditions.

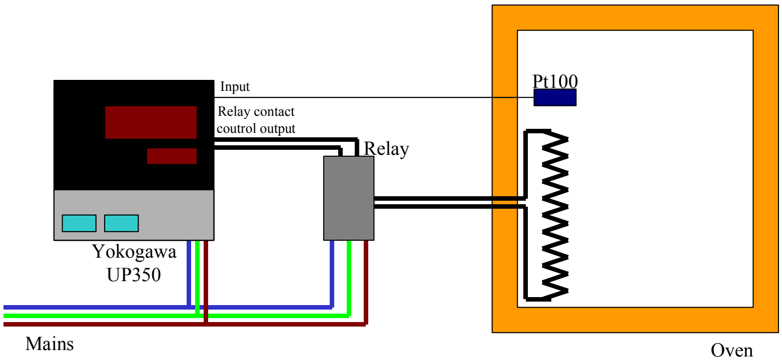

Fig. 97 : Annealing oven working principle.

The temperature uniformity is ensured by the fact that the heating resistor is in fact tied on the outer part of a steel enclosure (not shown on Fig. 97). This gives a very uniform heating inside the oven, at the position of the Pt100 sensor and where we perform the actual heat treatments. The design of the oven allows the heat treatment of either 6 standard CMS structures or 2 full-sized sensors.

A.2.2. Performances

The performances of the oven have been measured using a separate Pt100 read by a HP34970a data acquisition/switch unit.

Different tests have been carried out:

1. A maximum temperature test
2. A heating speed and stability test over more than 40 hours and for 2 different temperature settings (50 °C and 60 °C)
3. A temperature uniformity test over the 2 plateaus of the oven

The oven proved to hold temperatures up to 200 °C. Higher temperatures are possible with the replacement of the cabling for the Pt100 sensor.

On the other hand, the average heating speed from ambient to 50-60 °C appeared to be of 4 °C/min. This heating speed is practical, as one needs only 10 minutes to get the oven ready for annealing. The fluctuations of the temperature with time are about 0.3 °C on average with maximal deviations less than 2 °C. This test is illustrated on Fig. 98, where one clearly sees the oven stability in the 60 °C plateau.

Another parameter of importance is the temperature variation in the oven during openings (e.g.: at the beginning of the annealing). It can of course not be deduced from measurement shown on Fig. 98, because the opening of the oven remained closed during the entire test. Anyway, with the oven stabilised at 60 °C, opening the door during 1 min causes a drop of the temperature down to 57 °C, which is recovered in less than 2 min when the oven is closed again. If one leaves the oven open for a longer time (5 min), the regulation system will work in order to stabilize it at the nominal temperature setting, but this will result in a small overheating as the oven is closed again.

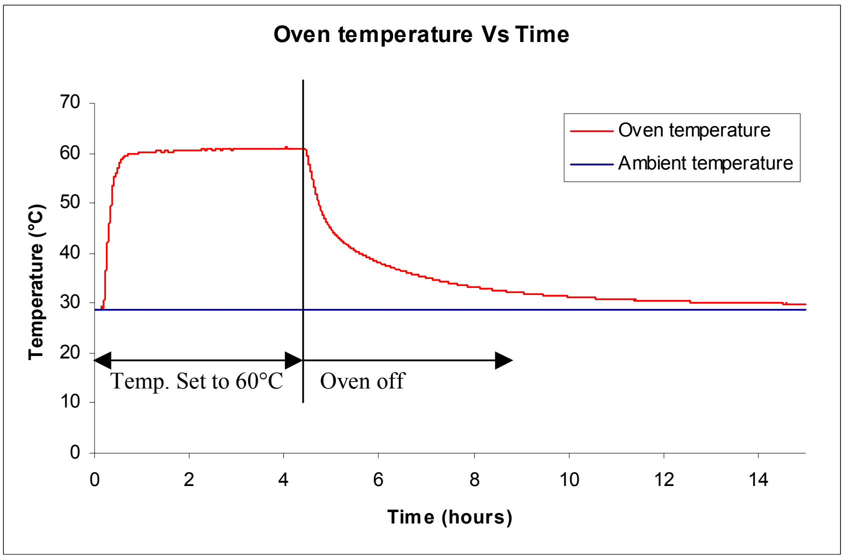

Fig. 98 : Temperature stability test at 60 °C (standard annealing temperature).

About the uniformity test, we placed Pt100 sensors at 12 different places on the 2 plates of the oven (6 on each, in 2 rows of 3 spots). The temperature deviation between the different measurements did not exceed 0.7 °C, proving the temperature is uniform enough.

A.3. Useful constants

A.3.1. Silicon properties

Gap (eV)	1.12
Gap variation as a function of temperature (eV/K)	$-2.30\ 10^{-4}$
Density of states in the conduction band - Nc ($1/cm^3$)	$2.8\text{-}3.22\ 10^{19}$
Density of states in the valence band - Nd ($1/cm^3$)	$1.04\text{-}1.83\ 10^{19}$
Electro affinity (eV)	4.05-4.85
Intrinsic charge carrier concentration ($1/cm^3$)	$1.02\text{-}1.4510^{10}$
Electron-hole pair creation mean energy (eV)	3.63
Fano factor	0.115
Intrinsic resistivity (Ω.cm)	$230\ 10^3$
Dielectric constant	11.9
Electron mobility μ_n (cm^2/V.s)	1450
Hole mobility μ_p (cm^2/V.s)	505
Electron saturation velocity $v_{s,n}$ (cm/s)	10^7
Hole saturation velocity $v_{s,p}$ (cm/s)	$8.4\ 10^6$
Breakdown voltage (V/cm)	$\sim 3\ 10^5$

Table 25 : Electrical properties of silicon crystal (at 300 K).

Structure	Diamond
Lattice (Angström)	5.431
Atomic number	14
Mean atomic mass	28.09
Density (g/cm^3)	2.329
Thermal expansion coefficient (1/K)	$2.56\ 10^{-6}$
Thermal conductivity (W/m.K)	1.53
Refraction index	3.42
Fusion temperature (°C)	1392-1415
Radiation length (cm) (g/cm^2)	9.36 21.82

Table 26 : Physical properties of Silicon

A.3.2. Silicon oxide properties (SiO_2)

Structure	Amorphous
Resistivity (Ω.cm)	10^{14}-10^{16}
Density (g/cm^3)	2.27
Dielectric constant	3.84
Breakdown voltage (V/cm)	$5\ 10^6$-$8\ 10^6$
Gap (eV)	8.8
Thermal expansion coefficient (1/K)	$5\ 10^{-7}$
Thermal conductivity (W/m.K)	0.014
Refraction index	1.46
Radiation length (cm) (g/cm^2)	10.2 27.05

Table 27 : Silicon oxide properties

Terms, abbreviations

Usual notations and sensor-related abbreviations:

C_{back} The backplane or bulk capacitance of the sensor. It is measured between the bias ring and the backplane.

q The proton charge, 1.6 10^{-19} C.

ε The relative dielectric constant of the medium (no units).

ε_0 The permittivity in vacuum, in Farads per unit length.

d The depletion zone thickness, in units of length. Sometimes confounded with the detector thickness in some equations where the sensor is depleted.

N_{eff} The effective doping concentration of the semiconductor, in particle per unit volume. It is the difference between the donor and acceptor concentrations.

V_{bi} The built-in voltage of a PN junction. It is the resulting electrical potential across the junction when no bias is applied. It results from the diffusion of electrons and holes.

V, V_{bias} Usually, the reverse voltage applied on the PN junction, diode or microstrip sensor.

V_{dep} The full depletion voltage of a device, it is reached as the depletion zone thickness is equal to the thickness of the sensor.

J_{leak} The leakage current surface density of a reverse-biased device.

I_{leak} The leakage current of a reverse-biased device.

d_{bi} The thickness of the built-in depletion zone

n_i The intrinsic carrier concentration, per unit volume.

τ_g The minority carrier generation lifetime.

p The pitch between two strips of a microstrip sensor.

w The width of the p+ implantation of a strip.

Φ_{eq} The 1-MeV equivalent fluence, as determined using the NIEL hypothesis (in particle per unit surface).

α The total leakage current of a device, divided by the volume of the junction and the 1-MeV equivalent fluence. In principle it is independent of the bulk type.

t_a	The annealing time.
T_a	The annealing temperature.
r	In equations related to the Hamburg Model, it is the donor removal constant (in fraction of the initial effective doping concentration).
g_c	The stable damage introduction rate (per unit fluence and volume).
g_a	The beneficial annealing defect introduction rate (per unit fluence and volume).
τ_a	The beneficial annealing time constant. As it is highly temperature-dependent, it is often accompanied by a temperature indication.
g_y	The reverse annealing defect introduction rate (per unit fluence and volume).
τ_y	The reverse annealing time constant. As it is highly temperature-dependent, it is often accompanied by a temperature indication.
C_{ac}	The coupling capacitance of a strip. it is measured between the DC pad (contact with the bias resistor and the p^+ implant) and AC pad (readout) of the strip.
R_{poly}	The bias resistor.
C_{int}	The interstrip capacitance. It is measured in between two adjacent strips.
R_{int}	The interstrip resistance. It is measured in between two adjacent strips.
R_{p+}	This is the measurement of the p^+ implant resistivity, in Ohm/cm, it is in fact a measurement of the doping concentration of the implant.
R_{Al}	It is the value of the resistivity of the aluminization layer, in Ohm/cm².
I_{diel}	The leakage current that passes trough the dielectric of an AC-coupled strip.
I_{strip}	The bulk-generated leakage current passing trough a given strip to the bias ring. In principle, it should correspond to the total leakage current of the detector, divided by the number of strips.
κ	the hardness factor of a beam or a particle at a given energy. It is the ratio between the 1-MeV equivalent fluence and the real fluence in the NIEL hypothesis.

Text abbreviations and some useful terms :

APV Analogue Pipeline Voltage, it is the front-end chip that keeps the bunch readouts, waiting for the level 1 trigger information in order to further keep the information or delete it.

CCU The Control Clock Unit distributes the bunch synchronisation information.

CV Capacitance-Voltage. The measurement of the bulk capacitance of a sensor as a function of the reverse bias voltage, useful to determine the full depletion voltage of a sensor.

DLTS Deep Level Transient Spectroscopy. This technique is useful for determining the type of defects induced in the bulk at the microscopic level. The very basic principle is to inject charge into the bulk in order to fill all traps. The measurement of the subsequent voltage or current transients following an abrupt change in the applied bias voltage are detected and analysed. This technique has the disadvantage that defect concentrations have to be kept low in order to not saturate the signal.

ECAL Electromagnetic Calorimeter

FEC Front End Controller, the module control electronic device.

FED Front End Driver, the module readout device

Float zone The float zone technique for growing silicon ingots uses. To get a detector-grade silicon ingot, a high-purity polycrystalline rod is re-melted into a monocristal ingot by being driven trough a RF coil. The RF coil is used to heat the rod locally and molten a "zone" of it. Hence the name. This technique performs also a simultaneous purification the crystal. Float zone (FZ) silicon presenting a low-level of impurity is often referred as standard Float zone (STFZ), whereas oxygen-doped silicon is mostly referred as diffusion-oxygenated float zone (DOFZ). Oxygenated float zone has shown an improved radiation-hardness to charged particle fluences.

Fluence The fluence (in $1/cm^2$) is the total integrated particle flux over a given period.

Frenkel Frenkel pairs are the most basic microscopic defects. It consist of a vacancy (V) –interstitial (I) pair, created together by the kick-out of a lattice atom out of its initial position.

GPIB The GPIB (general purpose interface bus) was specifically designed to connect computers, peripherals and laboratory instruments so that data and control information could pass between them. It is also known as IEEE-488 or HPIB and is the communication protocol we used to control the electrical characterization setup. It is faster than RS-232 and allow daisy-chaining of the instruments

HCAL Hadronic calorimeter

HIP Heavily Ionizing Particle: this kind of events present a very large ionizing energy deposition on a sensor. This kind of deposition can saturate the readout electronics and in fact acts like a “pinhole” (breakdown of the coupling capacitance dielectric).

HPK Hamamatsu Photonics company, one of the CMS silicon microstrip sensors manufacturer.

IQC Irradiation Qualification Center. The Louvain and Karlsruhe centres in charge of the routine irradiations for radiation hardness testing of the sensor production.

IV Current-voltage. It is the measurement of a sensor’s leakage current as a function of the reverse bias voltage.

LCR The abbreviation for a device able to measure inductance (L), capacitance (C) or resistance (R). This kind of equipment measures in fact the impedance of an electrical circuit at a given frequency and is thereafter able to assess the different components at the origin of the impedance.

LHC Large Hadron Collider.

MOS Metal Oxide Semiconductor device. This device , like its name suggests it, is made of a semincondutor bulk on top of which are stacked an oxide layer and a conductive layer (metal). It is characterized mainly by two working regime: depletion and accumulation. In the first regime, the semiconductor bulk is depleted (reverse-biased) and in the other, it is forward-biased and hence charge carriers accumulate at the oxide. The voltage at which the transition between the two modes occur is determined by the oxide quality: the less trapped charges, the closer to zero is this transition voltage.

MSSM The Mimimal Supersymmetric extension of the Standard Model is one of the model proposed as extension of the standard model. It assumes the existence of three neutral Higgses (A^0, H^0 and h^0) and two charged Higgses (H^+ and H^-).

NIEL Non-ionizong Energy Loss. It is the part of the energy deposition within a semiconductor device that is though to be at the origin of permanent damage in the device. The NIEL hypothesis assumes that the variation of the bulk electrical properties of a semiconductor device scales with this energy deposition.

Oxygenated Cf. float zone

PET The polyethylene used to make the support strip for our alanine dosimeters. It is widely used as material for plastic bottles.

PKA Primary Knock on Atom: it is the initial collision that removed a lattice atom from its position.

PQC Process Qualification Center. These centres, member of the silicon sensor group of the CMS Tracker collaboration performed measurements on test structures that were foreseen to monitor the consistency of the production quality of the sensors, by e.g. measuring the quality of the aluminium deposition.

PSI Paul Scherrer Institute.

QTC Quality Test Center. These centres, member of the silicon sensor group of the CMS Tracker collaboration performed measurements on the full-sized sensors in order to monitor the possible defects.

Rd48, ROSE

The so-called ROSE (Research and development On Silicon detectors for future Experiments) collaboration, now over, is one of the most fruitful collaboration about the radiation hardness of silicon sensors. It yields, for instance, the well known Hamburg model for the evolution of the effective doping concentration.

R.E. Relative effectiveness. It is a factor used to scale the response of dosimeter in a given radiation field.

SEE-SEU-SEL

Single Event Effects (SEE) are due toi the crossing of the detector by a single particle. These effects are classified according to their permanency into Dingle Event Upset (SEU) and Single Event Latchup (SEL).

A SEU is a soft, non-destructive error. Resetting the device affected ensures that it operates again in a normal way. Typical examples are pulses in analogic circuits or bit flips in digital devices.

A SEL causes a loss of device functionality. It is a hard error that potentially causes permanent damage. A typical example is the creation of high leakage channels resulting in currents above the device specifications.

ST ST microelectronics was the second provider of silicon sensors for CMS. It has been dismissed due to production problems.

Standard deviation

For a given set of measurements of average value μ, the standard deviation is given by the following expression:

$$\sigma = \sqrt{V} = \sqrt{\frac{\sum_{i=1}^{N}(x_i - \mu)^2}{N}}$$

Where V is called the Variance of the sample

Standard silicon Cf. Float zone

TEC Tracker EndCap. It is the forward parts of the tracker, where devices are arranged in wheels perpendicular to the beampipe.

TIB Tracker Inner Barrel. It is the inner part of the tracker, where 320 µm thick sensors are arranged in rods and facing the beampipe.

TOB Tracker Outer Barrel. It is the outer part of the tracker, where 500 µm thick sensors are arranged in rods and facing the beampipe.

TSC Thermally Stimulated Current. Like DLTS, it is a technique for investigating the microscopic defects induced in a silicon sensor. It has the advantage on DLTS that the defect concentration does not have to be low. The basic principle is to first cool down the sensor under reverse bias(or zero bias, depending on the measurement). Once cooled, charges are injected in the bulk trough forward bias or illumination. Thereafter, the device is heated at a constant temperature variation rate. Leakage current is monitored during the whole procedure and its variation with temperature is used to determine the levels and concentration of defects.

Bibliography

[1] "Radiation detection and measurement, third edition", G.F. Knoll, John Wiley & Sons, 1999.

[2] "Semiconductor radiation detectors – device physics", G. Lutz, Springer-Verlag, 1999.

[3] "The particle detector briefbook", R.K. Bock & A. Vasilescu, Springer-Verlag, 1998.

[4] "Physics of semiconductor devices, second edition", S.M. Sze, John Wiley & Sons, 1981.

[5] "Radiation hardness of silicon detectors – a challenge from High-Energy Physics", G. Lindström et al, Nucl. Instr. Meth. A vol. 426 (1-15), 1999.

[6] "Higgs coupling at the LHC",D. Zeppenfeld, HEP/PH0203123v1, 2006.

[7] "Physics at LHC", G. Wrochna, CMS CR 2002-015, CERN, 2002.

[8] "CMS Physics overview", C.-E. Wulz, CMS CR 2001-016, CERN, 2001.

[9] "Atlas detector and Physics performance, technical design report volume II", The Atlas Collaboration, CERN/LHCC 99-15, 1999.

[10] "Direct collider signatures of large extra-dimensions", I. Antoniadis et al., HEP-PH/9905311, 1999.

[11] "Indirect collider signals for extra-dimensions", J. L. Hewett, Phys. Rev. Let. 82-124, 1999.

[12] "CMS trigger strategies for the selection of MSSM Higgs boson using electron-tau decay modes", O. van der Aa, PhD thesis, UCL, 2005.

[13] The CMS letter of intent

[14] "The alignment system of the CMS tracker", A. Ostaptchouk et al, 2001.

[15] "The tracker project technical design report", the CMS collaboration, CERN/LHCC 98-6, 1998.

[16] "The tracker project technical design report addendum", the CMS collaboration, CERN/LHCC 2000-016, 2000.

[17] "Layout and performance of the CMS silicon strip tracker", D. Abbaneo, CMS CR 2003/032, 2003.

[18] "Radiation and temperature effects on the APV25 readout chip for the CMS tracker", E. Noah, PhD thesis, Imperial College of London, 2002.

[19] "CMS inner tracking",M. Manelli, Eur; Phys. J. C vol. 34, 2004.

[20] "Sensor alignment by tracks", V. Karimäki et al., CMS CR 2003-022, 2003.

[21] "R&D for the CMS silicon tracker", L. Feld, presentation shown on 15/01/1999 at CERN.

[22] "Notes on fluence normalisation based on the NIEL scaling hypothesis", A. Vasilescu & G. Lindström, ROSE/TN/2000/02, 2000.

[23] "Highly ionising events in silicon detectors", M. Huhtinen, CMS NOTE 2002-011, CERN, 2002.

[24] "The effect of highly ionising particles on the CMS silicon strip tracker", L. Mirabito et al., CMS NOTE 2004-011, CERN, 2004.

[25] "The NIEL hypothesis applied to neutron spectra of irradiation facilities and in the ATLAS and CMS SCT", A. Vasilescu, ROSE/TN/97-2, revised in December 1999.

[26] "Capacitances in silicon microstrip detectors", E. Barberis et al., Nucl. Instr. Meth. A vol. 342 (90-95), 1994.

[27] "Influence of the geometrical layout of the silicon microstrip detectors on electrical characteristics", T. Angelescu et al, EPPG/PHYS 38, 1998.

[28] "Les senseurs silicium pour CMS: caractérisation et mise en oeuvre des tests de résistance aux rayonnements", E. Forton, unpublished DEA report, 2001.

[29] "Nuclear electronics", E. Kowalski,Springer-Verlag, 1970.

[30] " Low noise techniques in detectors", V. Radeka, Ann. Rev. Nucl. Part. Sci. vo; 38 (217-277), 1988.

[31] "The impact of high-energy proton irradiation on the low frequency 1/*f* noise in FZ-silicon diodes", E. Simoen, C. Claeys, Mat. Sc. in Semic. Processing vol. 3, 2000.

[32] "Radiation damage in silicon detectors – microscopic defects and macroscopic properties", M. Moll, DESY-THESIS-1999-040, 1999.

[33] "Investigation of design parameters and choice of substrate resistivity and crystal orientation for the CMS silicon microstrip detector", S. Braibant et al, CMS note 2000/011.

[34] "Time development and flux dependence of neutron-irradiation induced defects in siliconpad detectors", D. Zontar et al., Nucl. Instr. Meth. A vol. 426, 1999.

[35] "Bias-dependent radiation damage in high-resistivity silicon diodes irradiated with heavy charged particles", V. Cindro et al, preprint, 1999.

[36] "Bias-dependent annealing of radiation damage in neutron-irradiated silicon p+ - n - n+ diodes", V. Cindro et al, Nucl. Instr. Meth. A vol. 419, 1998.

[37] "Bias dependence and bistability of radiation effects insilicon" , M. Mikuz et al, Nucl. Instr. Meth. A vol. 466, 2001.

[38] "Optimization of the silicon sensors for the CMS tracker", S. Albergo et al., Nucl. Instr. Meth. A vol. 466 (300-307), 2001.

[39] "Comprehensive study on theeffects of irradiation on charge collection efficiency in silicon detectors", L. Borello et al. , Nucl. Instr. Meth. A vol. 461 (178-181), 2001.

[40] "Simulation of non-ionising energy loss and defect formation in silicon", M. Huhtinen, ROSE/TN/2001-02, CERN, 2001.

[41] "Neutron displacement cross-sections for structural materials below 800 MeV", A. Yu Konobeyev et al. , Journal of nuclear Physics vol. 186 (117-130), 1992.

[42] "Displacement damage in silicon", A. Vasilescu & G. Lindström, on-line compilation available at http://sesam.desy.de/~gunnar/Si-dfuncs.

[43] "Observation of a bistable defect generated and activated by heat treatments in irradiated high resistivity silicon detectors", M. Moll et al., Nuclear Physcics B (proc. suppl.) vol. 44 (468-474), 1995.

[44] "Results since last workshop", A. Furgeri, private communication at the "2nd IQC workshop" held in Louvain-la-Neuve in May 2003.

[45] "The silicon sensors for the Compact Muon Solenoid tracker – design and qualification procedure", J.-L. Agram et al, Nucl. Instr. Meth. A vol. 517 (77-93), 2004.

[46] "Specifications for the Quality Control & Assurance of the CMS Silicon Sensors", the CMS Tracker sensor Working Group, unpublished, 2000.

[47] "Sensors and modules under mechanical stress", F. Hartmann, presentation at the "STM mini-workshop", CERN, December 2003.

[48] “Etude du comportement de détecteurs gazeux à micro-pistes MSGC sous irradiation intense de neutrons rapides ”, K. Bernier, PhD thesis, UCL, 2001.
[49] “An intense fast neutron beam in Louvain-la-Neuve”, K. Bernier et al, available on the web at http://www.fynu.ucl.ac.be/themes/he/cms/neutron_beam/neutrons-beam.html .
[50] Yokogawa UP14 manual
[51] “Radiation damage in silicon detectors – an introduction for non-specialists”, M. Moll, CERN EP-TA1-SD seminar 14/02/2002, transparencies available on the web.
[52] "Results on radiation hardness of silicon strip detectors up to neutron fluences of 10^15 n/cm2", R. Wunstorf & M. Benkert, Nucl. Instr. Meth. A vol. 315, 1992.
[53] “Experimental cross sections for light-charged particle production induced by neutrons with energies between 25 and 65 MeV incident on oxygen”, S. Benck et al, Atomic data and nuclear data tables 72 (1-20), 1999.
[54] “Quasi-monoenergetic neutron beams with energies from 25 to 70 MeV”, H. Schuhmacher et al, Nucl. Instr. Meth. A vol. 421 (284-295), 1999.
[55] Private discussion with G. Lindström about the monoenergetic neutron beam test.
[56] “Standard guide for selection and use of neutrons sensors for determining neutron spectra employed in radiation hardness testing of electronics”, ASTM note E 720-02.
[57] “Dosimetry by ESR spectroscopy of alanine”, D.F.Regulla & U. Deffner, Int; J. Appl. Radiat. Isot. vol.33 (1101-1114), 1982.
[58] “Intercomparison of gamma ray, X ray, and fast neutron dosimetry using alanine detectors”, J.W. Hansen et al, Rad. Prot. Dosimetry vol. 27 N°2 (85-92), 1989.
[59] “Data compilation of dosimetry methods and radiation sources for material testing”, M. Tavlet et al, CERN/TIS-CFM/IR/93-03, 1993.
[60] “A consistent set of neutron kerma coefficients from thermal to 150 MeV for biologically important materials”, M.B. Chadwick et al., Med. Phys. vol 26 N°6 (974-991), 1999.
[61] “Experimental kerma coefficients of biologically important materials at neutron energies below 75 MeV” , J.P. Meulders et al., Med. Phys. vol 27 N°11 (2541-2559), 2000.
[62] “The response of the alanine detector after charged-particle and neutron irradiations”, M.P.R. Waligorski et al, Appl. Radiat. Isot vol 40 (923-933), 1989.
[63] “Calculations of the relative effectiveness of alanine for neutrons with energies up to 17,1 MeV”, H.M. Gertsenberg, Rad; Prot. Dosimetry vol.31 N°1/4 (85-89), 1990.
[64] “Fast neutron response of alanine probes”, H. Schraube et al, Appl. Radiat. Isot vol 40 (941-944), 1989.
[65] “Radioactivity and radiation protection”, R.J. Donahue & A Fasso in the particle data group booklet.
[66] “Standard practice for use of the alanine-EPR dosimetry system”, ASTM note E 1607-96.
[67] “The response of the alanine dosemeter to low energy protons and high energy heavy charged particles”, K.J. Olsen & J.W. Hansen, Radiat. prot. dosimetry vol 31 (81-84), 1990.
[68] “Proton response of alanine based pellets and films”, S. Onori et al, Appl. Radiat. Isot vol 47 (1201-1204), 1996.
[69] “Alanine EPR dosimeter response in proton therapy beams”, K. Gall et al, Appl. Radiat. Isot vol 47 (1197-1199), 1996.

[70] "Response characteristics of thermoluminescence and alanine-based dosemeters to 16 and 25 MeV proton beams", A. Bartolotta et al, Radiat. prot. dosimetry vol 85 (353-356), 1999.

[71] "UP350 Program Controller Instruction Manual", Yokogawa M&C Corporation, 1-19-18 Nakacho, Musashino-shi, Tokyo 180-0006, JAPAN.

List of figures

List of tables